Numerical Investigation of Shell Formation in Thin Slab Casting of Funnel-Type Mold

A. VAKHRUSHEV, M. WU, A. LUDWIG, Y. TANG, G. HACKL, and G. NITZL

The key issue for modeling thin slab casting (TSC) process is to consider the evolution of the solid shell including fully solidified strand and partially solidified dendritic mushy zone, which strongly interacts with the turbulent flow and in the meantime is subject to continuous deformation due to the funnel-type mold. Here an enthalpy-based mixture solidification model that considers turbulent flow [Prescott and Incropera, *ASME HTD*, 1994, vol. 280, pp. 59–69] is employed and further enhanced by including the motion of the solidifying and deforming solid shell. The motion of the solid phase is calculated with an incompressible rigid viscoplastic model on the basis of an assumed moving boundary velocity condition. In the first part, a 2D benchmark is simulated to mimic the solidification and motion of the solid shell. The importance of numerical treatment of the advection of latent heat in the deforming solid shell (mushy zone) is specially addressed, and some interesting phenomena of interaction between the turbulent flow and the growing mushy zone are presented. In the second part, an example of 3D TSC is presented to demonstrate the model suitability. Finally, techniques for the improvement of calculation accuracy and computation efficiency as well as experimental evaluations are also discussed.

DOI: 10.1007/s11663-014-0030-2

I. INTRODUCTION

THIN slab casting (TSC) is increasingly implemented, in competition with conventional slab casting, for producing flat/strip products due to its advantages of integrating the casting-rolling production chain, energy saving, high productivity, and near net shape.[1,2] However, problems such as the sensitivity to breakout and edge/surface cracks were frequently reported. These problems have encouraged metallurgists to consider a special mold design,[3–5] cooling system, and submerge entry nozzle (SEN)[6–8] to use a special mold flux[9] and even to apply electromagnetic braking in the mold region.[7,8,10] The modeling approach becomes a useful tool to assist the system design.[5–8,10–18] One striking feature of TSC, different from that of conventional slab casting, is the use of the funnel-type mold, which provides the necessary space for the SEN to conduct liquid melt into the thin slab mold. Another important feature is the shell thickness which solidifies in the mold region: 40 to 50 pct of the slab thickness for TSC.[3] In comparison, there is only 20 to 30 pct of slab thickness which solidifies in the mold region for the conventional slab.[19,20] Therefore, the evolution of solid shell under the influence of turbulent flow and subject to the continuous shell deformation in TSC becomes a critical issue for the modeling approach.

Different models were used to calculate solidification of TSC. One of these is the so-called 'equivalent heat capacity model', as proposed by Hsiao.[21] This model was originally proposed for the solidification without solid motion, as the transport of latent heat in the mushy zone due to the motion of the solid phase is not considered. According to recent investigations,[22,23] the transport of latent heat in the moving (deforming) mushy zone plays a very important part in continuously cast and solidified objects, *e.g.*, continuous casting. The treatment of the motion of the solid phase has a significant influence on the advection of the latent heat, and hence on the evolution of the mushy zone. In order to consider the advection of latent heat under the condition of deforming and moving mushy zone, an enthalpy-based mixture solidification model is favored.[24–26] Another feature of the enthalpy-based model is to provide a possibility to consider the flow–solidification interaction in the mushy zone by introducing a volume-averaged parameter, *i.e.*, permeability. The drag of the dendritic network of the crystals in the mush to the interdendritic flow is considered by the permeability, which is a function of the local solid fraction and the microstructural parameters such as the primary dendrite arm space. This model was later extended by including the model of turbulence,[27–30] and applied to study the solidification and formation of macrosegregation under the influence of forced convection.

A. VAKHRUSHEV, Senior Researcher, is with the Christian-Doppler Lab for Adv. Process Simulation of Solidification & Melting, Department of Metallurgy, University of Leoben, Franz-Josef-Str. 18, 8700 Leoben, Austria. M. WU, Associate Professor, is with the Christian-Doppler Lab for Adv. Process Simulation of Solidification & Melting, Department of Metallurgy, University of Leoben, and also Department of Metallurgy, University of Leoben. Contact e-mail: menghuai.wu@unileoben.ac.at A. LUDWIG, University Professor, is with the Department of Metallurgy, University of Leoben. Y. TANG and G. HACKL, Project Managers, are with the RHI AG, Technology Center, Magnesitstrasse 2, 8700 Leoben, Austria. G. NITZL, Product Manager, is with the RHI AG, Wienerbergstrasse 9, 1100 Vienna, Austria.

Manuscript submitted July 3, 2013.
Article published online February 20, 2014.

The enthalpy-based mixture solidification model considering turbulent flow[27–30] was previously used by the current authors to model conventional continuous casting,[19] where the motion of the solid shell was assumed to be parallel, and the moving velocity is constant everywhere and equal to the casting velocity. No thermal mechanical model is used and the gap formation between the solid strand and the mold is not explicitly modeled, but the reduction of heat transfer at the strand–mold interface due to the formation of gap is considered by an experimentally determined or an empirical distribution profile of heat flux at the strand–mold interface along the casting direction. Evidently, the assumption of parallel motion and constant velocity of the solid does not apply to TSC, where the strand shell is subject to continuous deformation due to the funnel-type mold. Despite the same consideration of the experimentally determined heat flux, the use of the funnel-type mold must be treated properly, because it guides the motion of the solid shell of the strand and influences the melt flow inside the strand. Therefore, the objectives of the present work were (1) to extend the previous model by considering the deforming solid shell; (2) to explore some flow–solidification interaction phenomena during solidification of TSC; (3) to demonstrate the importance of numerical treatment of the advection of latent heat; (4) and to examine the suitability of the model for TSC in respect of the calculation accuracy and computational efficiency.

II. MODEL DESCRIPTION

A. *Solidification and Turbulence Flow*

An enthalpy-based mixture solidification model[24–26] is applied. As shown in Figure 1, this mixture combines a liquid ℓ-phase and solid s-phase. They are quantified by their volume fractions, f_ℓ and f_s, and $f_\ell + f_\mathrm{s} = 1$. The morphology of the solid phase is usually dendritic, but here we consider the dendritic solid phase as part of the mixture continuum. The flow in the mushy zone is determined according to permeability, while the motion of solid phase is estimated. Free motion of crystals (equiaxed) is ignored. The mixture continuum changes continuously from a pure liquid region, through the mushy zone (two-phase region), to the complete solid region. The evolution of the solid phase is determined by the temperature according to a f_s–T relation. Different analytical models[31] for the f_s–T relation are available. To evaluate the numerical model solidification of a 2D benchmark casting of a Fe-C binary alloy is calculated (Section III). The f_s–T relation according to lever rule is applied because the alloy element C in both liquid and solid phases of Fe-C alloy is very diffusive, and the solidification path of the Fe-C binary alloy is more consistent with the model of lever rule:

$$f_\mathrm{s} = \begin{cases} 0 & T > T_\mathrm{liquidus} \\ \left(T_\mathrm{liquidus} - T\right)/\left(\left(T_\mathrm{f} - T\right)\cdot\left(1 - k_\mathrm{p}\right)\right) & T_\mathrm{liquidus} \geq T > T_\mathrm{solidus} \\ 1 & T_\mathrm{solidus} \leq T. \end{cases} \quad [1]$$

For the calculation of solidification of industry alloy (Section IV), another f_s–T relation, determined by engineering software IDS,[32] is used. Only one set of Navier–Stokes equations, which apply to the domain of the bulk melt and mushy zone, are solved in the Eulerian frame of reference.

$$\nabla \cdot \vec{u} = 0, \quad [2]$$

$$\rho \frac{\partial \vec{u}}{\partial t} + \rho \nabla \cdot \left(\vec{u} \otimes \vec{u}\right) = -\nabla p + \nabla \cdot (\mu_\mathrm{eff} \nabla \vec{u}) + \vec{S}_\mathrm{mom}, \quad [3]$$

$$\text{where } \vec{u} = \begin{cases} \vec{u}_\ell & \text{bulk melt region} \\ f_\ell \vec{u}_\ell + f_\mathrm{s} \vec{u}_\mathrm{s} & \text{mushy zone} \\ \vec{u}_\mathrm{s} & \text{solid region.} \end{cases} \quad [4]$$

The densities of both liquid and solid are treated as constant and equal. The drop in momentum due to the drag of the solid dendrites in the mushy zone is modeled by Darcy's law:

$$\vec{S}_\mathrm{mon} = -\frac{\mu_\ell}{K} \cdot (\vec{u} - \vec{u}_\mathrm{s}), \quad [5]$$

with the Blake–Kozeny approach for the permeability of the mush:[33]

$$K = \frac{f_\ell^3}{f_\mathrm{s}^2} \cdot 6 \cdot 10^{-4} \cdot \mathrm{PDAS}^2. \quad [6]$$

Here PDAS is the primary dendrite arm spacing which is assumed to be given and constant. The enthalpy-based energy conservation equation applies to the entire domain,

$$\rho \frac{\partial h}{\partial t} + \rho \nabla \cdot \left(\vec{u} h\right) = \nabla \cdot \lambda_\mathrm{eff} \nabla T + S_\mathrm{e}. \quad [7]$$

Here h is the sensible enthalpy of the mixture (better written as $h_\mathrm{mixture}^\mathrm{sensible}$, but for simplicity, the subscripts and superscripts are omitted). We assume that both liquid and solid phases have the same sensible enthalpy, $h_\ell^\mathrm{sensible} = h_s^\mathrm{sensible}$, which is equal to h as calculated by $h_\mathrm{ref} + \int_{T_\mathrm{ref}}^{T} c_\mathrm{p} \mathrm{d}T$. The total enthalpy of pure solid is equal to its sensible enthalpy, $h_\mathrm{s}^\mathrm{total} = h$; the total enthalpy of pure liquid is equal to the sum of its sensible enthalpy and latent heat (solidification heat of fusion, L), *i.e.*, $H_\ell = h + L$; the total enthalpy of the liquid–solid mixture (mushy zone) is calculated as $H = h + f_\ell L$. Equation (7) explicitly calculates the transport of the sensible enthalpy. The release of latent heat due to solidification and the advection of the latent heat are represented with the source term S_e

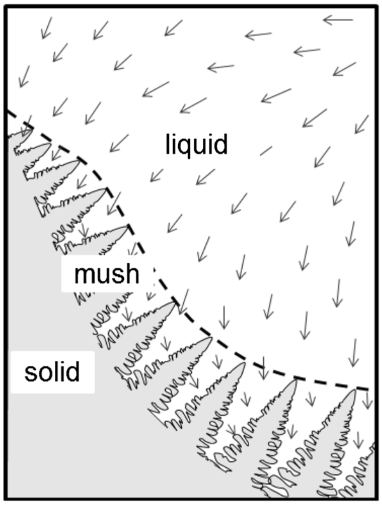

Fig. 1—Schematic of the solidifying mushy zone.

$$S_e = \rho L \partial f_s/\partial t - \rho L \nabla \cdot \left(f_\ell \vec{u}_\ell \right), \quad [8a]$$

or written as $$S_e = \rho L \partial f_s/\partial t + \rho L \nabla \cdot \left(f_s \vec{u}_s \right). \quad [8b]$$

A low Reynolds no. k–ε model was introduced by Prescott and Incropera[27–30] to calculate the turbulence kinetic energy k and turbulence dissipation rate ε during solidification. In current studies, a realizable k-ε model was employed, providing improved performance for flow calculations involving boundary layers under strong pressure gradients and strong streamline curvature. The governing equations for the turbulence are

$$\frac{\partial(\rho k)}{\partial t} + \nabla \cdot \left(\rho \vec{u} k \right) = \nabla \cdot \left(\left(\mu_\ell + \frac{\mu_t}{\mathrm{Pr}_{t,k}} \right) \nabla k \right) + G - \rho\varepsilon - \frac{\mu_\ell}{K} \cdot k, \quad [9]$$

$$\frac{\partial(\rho \varepsilon)}{\partial t} + \nabla \cdot \left(\rho \vec{u} \varepsilon \right) = \nabla \cdot \left(\left(\mu_\ell + \frac{\mu_t}{\mathrm{Pr}_{t,\varepsilon}} \right) \nabla \varepsilon \right) + \rho C_{1\varepsilon} S \varepsilon - C_{2\varepsilon} \rho \frac{\varepsilon^2}{k + \sqrt{S \cdot k}}, \quad [10]$$

The turbulence Prandtl no. for k is given as $\mathrm{Pr}_{t,k} = 1.0$ and for ε is given as $\mathrm{Pr}_{t,\varepsilon} = 1.2$. In Eq. [9], G is the shear production of turbulence kinetic energy, and in Eq. [10], $S = \sqrt{2 S_{ij} S_{ij}}$, where $S_{ij} = 0.5(\partial u_j/\partial x_i + \partial u_i/\partial x_j)$. A simple approach is used to modify the turbulence kinetic energy in the mushy zone. It is assumed that within a coherent mushy zone, turbulence is dampened by the shear resistance, which is linearly correlated with the reduction of the mush permeability. The influence of turbulence on the momentum and energy transports is considered by the effective viscosity, $\mu_{\mathrm{eff}} = \mu_\ell + \mu_t$, and the effective thermal conductivity, $\lambda_{\mathrm{eff}} = \lambda_{\mathrm{mix}} + \lambda_t$, where $\mu_t = \rho C_\mu k^2/\varepsilon$, $\lambda_{\mathrm{mix}} = f_\ell \lambda_\ell + f_s \lambda_s$, $\lambda_t = f_\ell \mu_t c_{p,\ell}/\mathrm{Pr}_{t,h}$, C_μ is a function of the velocity gradient and ensures positivity of normal stresses; $\mathrm{Pr}_{t,h}$ is the turbulence Prandtl no. for the energy equation ($\mathrm{Pr}_{t,h} = 0.85$).

The governing equations of the mixture solidification model above were implemented in an OpenFOAM® CFD software package.[34]

B. *Solid Velocity*

A simple incompressible rigid viscoplastic model is derived to estimate the solid velocity $\vec{u}_s$. The linear elasticity model[35] is simplified to the Navier–Cauchy equation:

$$(\lambda + \mu) \nabla \left(\nabla \cdot \vec{\delta} \right) + \mu \nabla \cdot \nabla \vec{\delta} = 0, \quad [11]$$

where $\vec{\delta}$ is the displacement vector. The so-called Lamé parameters λ and μ are

$$\lambda = \frac{E v}{(1+v)(1-2v)}, \quad \mu = \frac{E}{2(1+v)}, \quad [12]$$

where E represents Young's modulus and v is the Poisson's ratio. If the solid shell is incompressible ($v = 0.5$) and its strain is small, then a volume conservation condition is fulfilled:

$$\nabla \cdot \vec{\delta} = 0, \quad [13]$$

so the first term of Eq. [11] vanishes, and Eq. [11] is reduced to:

$$\nabla \cdot \nabla \vec{\delta} = 0. \quad [14]$$

By considering $\vec{u}_s = \partial \vec{\delta} \big/ \partial t$, we obtain the volume-conserved Laplace's equations:

$$\begin{cases} \nabla \cdot \nabla \vec{u}_s = 0, \\ \nabla \cdot \vec{u}_s = 0. \end{cases} \quad [15]$$

These volume-conserved Laplace's equations can be solved in two different ways: with a ω–ψ function method (Method I),[36] or by solving one-phase Navier–Stokes equations with an 'infinite (10^8 times of liquid viscosity) solid viscosity' (Method II). Method I provides a precise solution, but the algorithm for solving the ω–ψ function applies only to the 2D case. Method II applies to both the 2D and 3D cases, but it is only an approximation. A previous study[37] on a 2D benchmark has revealed that the maximum error of the estimated solid velocity by Method II is less than 1 pct. Therefore, in this study, we use Method II to estimate the solid velocity.

III. 2D BENCHMARK

A. *Benchmark Configuration*

A 2D benchmark is configured, as shown in Figure 2. The casting section is gradually reduced in a sinuous form to mimic the converged inner mold region (funnel shape) of TSC. Two-step calculations are made: (1) one for the solid velocity and (2) one for the flow and solidification. Mesh adaptation technique is used. The calculation starts with an initial mesh size of 1 mm. The mesh size is gradually refined to a mesh size of 0.25 mm in the vicinity of solidification front until the solidification result does not change anymore with further mesh refinement.

For the calculation of solid velocity, the calculation domain is further considered in two parts: one part is filled with a 'solid shell' and the remaining part is filled with liquid melt. The boundary conditions for the 'solid shell' are shown in Figure 2(a). The solid strand is drawn at the bottom with a constant velocity of $\vec{u}_{\mathrm{pull}} = 0.07\,\mathrm{m/s}$. A zero-gradient condition ($\nabla_{\mathrm{n}}\vec{u}_{\mathrm{s}} = 0$) is applied at the top boundary and at the second half of the outlet (bottom). The moving surface velocity is calculated with the assumption of a constant tangential moving velocity equal to $\vec{u}_{\mathrm{pull}}$:[18]

$$\vec{u}_{\mathrm{s}}^{\mathrm{surface}} = \left|\vec{u}_{\mathrm{pull}}\right| \cdot \frac{\vec{n}_{\mathrm{z}} - \left(\vec{n}_{\mathrm{z}} \cdot \vec{n}_{\mathrm{z}}\right) \cdot \vec{n}_{\mathrm{f}}}{\left|\vec{n}_{\mathrm{z}} - \left(\vec{n}_{\mathrm{z}} \cdot \vec{n}_{\mathrm{f}}\right) \cdot \vec{n}_{\mathrm{f}}\right|}, \qquad [16]$$

where $\vec{n}_{\mathrm{z}}$ and $\vec{n}_{\mathrm{f}}$ are unit vectors: one in the casting direction and one normal to the curved surface.

For the calculation of flow–solidification, the thermal and flow boundary conditions are shown in Figure 2(b). The melt with nominal composition of Fe—0.34 mass pct C fills continuously through the inlet (extra opening of 10 mm on the symmetry plane) into the domain with a constant temperature [1850 K (1577 °C)] and a constant pressure of atmosphere. A constant turbulence kinetic energy (2.5×10^{-4}) and constant dissipation rate (9.3×10^{-4}) are applied at the pressure inlet. A constant pull velocity $\vec{u}_{\mathrm{pull}}$ is applied at the outlet (bottom). The thermal boundary condition for the top (meniscus) and upper part of the mold is isolated, and flow boundary conditions are zero-stress. For the lower part of the mold, a convective heat transfer boundary condition is applied, and the flow boundary condition is zero-stress as well. Note that the configuration of this benchmark is to model some features of TSC, but not to replicate the real industry process. For example, the design of a pressure inlet at the symmetry plane is to catch some relevant phenomena of the jet flow, which conducts liquid melt into the casting domain and interacts with the mushy zone.

Other material properties are listed in Table I. In order to investigate the influence of the flow (turbulence, jet impingement) and the treatment of the advection of latent heat on the formation of the solid shell, 4 simulations are presented, as listed in Table II.

B. *Simulation Results*

Transient calculations are performed, but only steady-state results are presented. The flow is turbulent, and Reynolds no. is 8500. Figure 3 shows the calculated velocity fields of Case I. The solid velocity is almost parallel to the curved mold surface, while the liquid velocity shows a typical double roll flow pattern. A jet flow coming from the inlet impinges on the solidification front, and the solidification front is slightly concaved at the impingement point. Figure 3(c) shows the details of the flow near and in the mushy zone. The flow can penetrate into the mush, but the interdendritic flow is significantly 'dampened' in the vicinity of the solidification front. As expressed by Eq. [6], the permeability of the mushy zone drops with the increase of f_{s}. The permeability is also a function of primary dendrite arm space (PDAS). One can expect that a larger PDAS would lead to a deeper penetration of the flow into the mush, but the study regarding the influence of PDAS on the solidification in detail is out of the scope of the current paper.

Analyses of the solid-phase distributions along Paths I, II, and III, as marked in Figure 3(a), are made in Figure 4. The paths are 135, 192 and 518 mm distant from top surface, respectively. All calculation cases are compared. The total solid phase formed in the calculation domain, $f_{\mathrm{s}}^{\mathrm{integral}}$, is summarized in Table II. Evidently, the treatment of the advection of latent heat in the energy equation is verified to be extremely important. Disregarding the advection term, $\rho L \nabla \cdot \left(f_{\mathrm{s}}\vec{u}_{\mathrm{s}}\right)$, in Case II will to a great extent overestimate the solid shell thickness. According to the calculated $f_{\mathrm{s}}^{\mathrm{integral}}$ (Table II), the overestimation of the total solid phase formed in the whole calculation domain is (13.31–7.94)/7.94 × 100 pct = 67.6 pct. This overestimation can also be seen in Figure 4 as a comparison between Case I and II.

Case III is calculated without considering the side jet. The liquid melt is conducted into the domain from the top. The flow becomes calmer with a smaller Reynolds no. of 3100. The calculated shell profile of Case III is compared with that of Case I in Figures 4 and 5. It is obvious that without the side jet the shell grows thicker. According to the calculated $f_{\mathrm{s}}^{\mathrm{integral}}$, the total solid phase formed in Case III is predicted to be (9.51–7.94)/7.94 × 100 pct = 19.8 pct more than that in Case I. The influence of jet flow on the solidification can be attributed to two aspects: one is the transport of superheat by the jet flow to the solidification front leading to local remelting[38] and one is the jet-induced turbulence, which enhances the diffusion of the superheat from the bulk melt into the mushy zone.

To improve the understanding of the jet-induced turbulence and its influence on the shell formation, Figure 6 shows some relevant turbulence quantities of Case I. The calculated k and ε are small in the upper bulk region, but they are significantly increased in/near the front of the mushy zone, especially near the flow-jet impingement region and in the downstream region. The turbulence promotes thermal mixing and the effective thermal conductivity increases. $\lambda_{\mathrm{eff}}/\lambda_{\ell}$ reaches a factor of 30 to 40 in some regions. If λ_{eff} is increased by the turbulence, the transport of superheat from the jet flow to the solidification front is enhanced. It hints that the turbulence-induced mixing might suppress the solidification. To further verify this hypothesis, a Case IV is calculated. Case IV just repeats Case I, but in the energy conservation equation, Eq. [7], the contribution of the

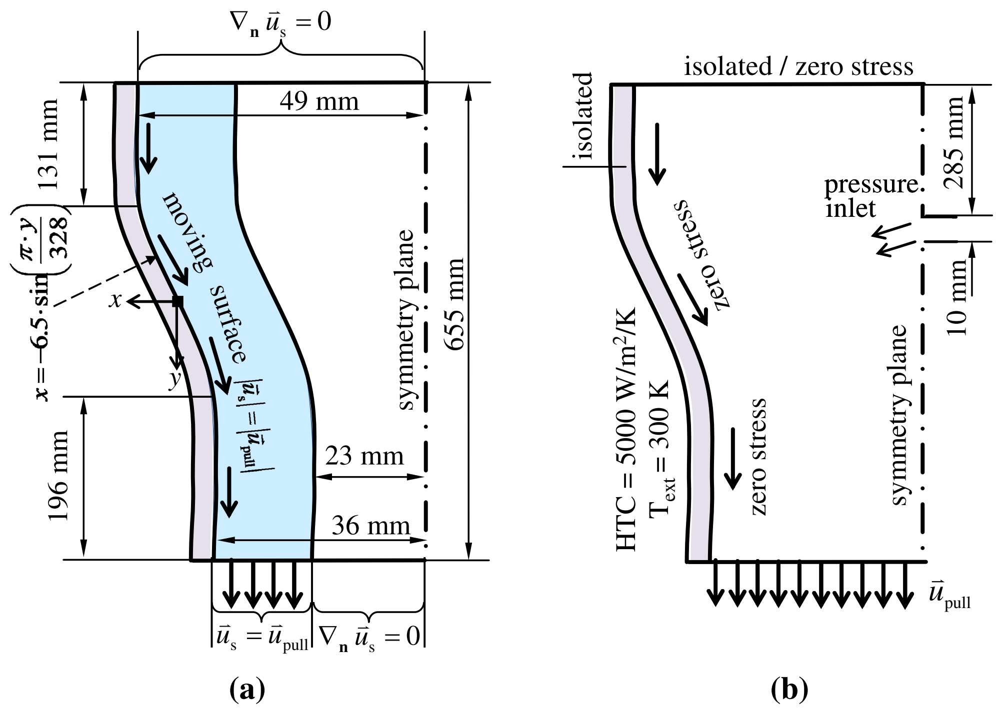

Fig. 2—Configuration of a 2D benchmark (*a*) for solid velocity calculation and (*b*) for the solidification–flow calculation. The geometry in the vertical direction is scaled by 1/8.

Table I. Properties and Parameters for the Calculations of the 2D Benchmark (Fe-0.34 mass pct C)

Thermal Physical Properties	Thermodynamic Data
c_p = 808.25 J kg^{-1} K^{-1}	c_0 = 0.34 mass pct C
λ_{mix} = 33.94 W m^{-1} K^{-1}	k_p = 0.2894
ρ = 7027 kg m^{-3}	T_f = 1811 K (1538 °C)
μ_ℓ = 5.6 × 10^{-3} kg m^{-1} s^{-1}	$T_{liquidus}$ = 1781.8 K (1508.8 °C)
L = 2.5 × 10^5 J kg^{-1}	$T_{solidus}$ = 1710.8 K (1687.8 °C)
Other Parameters	
PDAS = 4 × 10^{-4} m	
T_{inlet} = 1850 K (1577 °C)	
$\vec{u}_{pull} = 0.07\,\mathrm{m\,s^{-1}}$	

Table II. Parameter Study of the Flow–Solidification Interaction

	Jet Flow	Source Term of Latent Heat	$f_s^{integral}$ (vol pct)***
Case I	yes	S_e	7.94
Case II	yes	disregarding $\rho L \nabla \cdot \left(f_s \vec{u}_s\right)$ in S_e	13.31
Case III*	no	S_e	9.51
Case IV**	yes	S_e	9.55

*In Case III, the inlet boundary condition is modified. A pressure inlet is applied at the top boundary, and no side jet is considered.

**Case IV is identical to Case I, but in the energy conservation equation, Eq. [7], the contribution of the turbulence to the effective thermal conductivity is ignored, *i.e.*, $\lambda_{eff} = \lambda_{mix} + \lambda_t$, where $\lambda_t \equiv 0$.

***$f_s^{integral}$: Total solid phase (vol pct) in the whole calculation domain after reaching a steady-state solution.

turbulence to the effective thermal conductivity is ignored, *i.e.*, $\lambda_{eff} = \lambda_{mix} + \lambda_t$, where $\lambda_t \equiv 0$. The result of Case IV is compared with other cases in Figures 4 and 5. If the turbulence-enhanced thermal conductivity (λ_t) is dropped out, the result will become close to that of Case III. In other words, the developed shell profile of Case III without side jet and with less turbulence is compatible with that of Case IV with side jet and higher turbulence but ignoring the turbulence-induced thermal mixing. In the current benchmark, we find that the effect of turbulence-induced thermal mixing (enhanced thermal conductivity) seems to play more important role in the formation of shell thickness than the effect of transport of superheat by the jet flow in the presented benchmark case.

IV. THIN SLAB CASTING

The simulation of the TSC of low alloy steel, as shown in Figure 7, is performed. The composition of the alloy in mass pct is 0.06C, 0.1Ni, 0.13Mn, 0.1Si, 0.08Cu, 0.035Al, 0.015P, and 0.012S. The calculation domain includes a four-port submerged entry nozzle (SEN) and the entire mold region and a part of the water-cooled strand up to 2000 mm from the meniscus. The casting temperature is T_{inlet} = 1825 K (1552 °C) and the casting velocity is $\vec{u}_{pull} = 0.071\,\mathrm{m\,s^{-1}}$. As shown in Figure 8, the thermal physical properties and the f_s–T correlation are determined by an engineering software IDS.[32] For other properties/parameters such as ρ, L, μ_ℓ, and PDAS, refer to Table I. The moving surface velocity, calculated based on an assumption of a constant tangential moving velocity equal to $\vec{u}_{pull}$,[18] is set as moving boundary condition for the wide face (Figure 9). The heat flux boundary condition in mold for the wide face is taken from the literature[3], and for the narrow face, a constant heat flux (2.41 MW/m^2) is applied, while a constant heat transfer coefficient (1100 W/m^2 K) for the boundary (wide and narrow faces) below the mold exit is applied. To ensure the calculation accuracy, numerical techniques such as mesh adaptation are applied.[37,39] The calculation starts with an initial cell size of 2 mm (cells: 0.6 million), but during calculation, the cell size in the critical mushy zone is adapted to as small as 0.4 mm (cells: 4 million). All simulations were run in parallel on 8 CPUs (Intel Nehalem Cluster 2.93 GHz), and the calculation of a transient TSC process of 100 seconds took 2 weeks.

Flow simulation results are shown in Figure 10. With the four-port SEN, 4 convection rolls are developed. Roll **A** continuously transports superheat into the meniscus region to maintain a sufficiently high temperature and avoid premature solidification of the meniscus. Roll **B** creates a motion of meniscus toward the narrow face. This motion of meniscus is supposed to drag the liquid covering slag with it and facilitate the infiltration of the liquid slag into the gap to form a slag film between the strand and the mold. Rolls **C** and **D** promote the mixing of superheat in the wide face region, hence enhancing uniformity of the shell in the wide face region. The further merits of using the four-port SEN design regarding the optimization of the flow pattern have previously been studied.[6]

Figure 11 shows some details of flow–solidification interaction near the narrow face. A good resolution of the solidifying mushy zone is ensured with the help of numerical mesh adaptation. In the vicinity of the side jet impingement point, there are still ca. 6 grid points in the mushy zone. Shell formation is strongly influenced by the flow–solidification interactions. These interactions include the resistance of the solid dendrites (here treated as porous mushy zone) to the interdendritic flow and the transport of the superheat and latent heat of the liquid phase by the interdendritic flow. The moving solid phase in mushy zone impedes the bulk flow, slowing down the bulk flow gradually through the mushy zone to the shell moving velocity ($u^y = -0.071$ m/s). The velocity of the side jet is significantly reduced when reaching narrow face; the reduction of the solidification rate at the solidification front due to the impingement of the side jet is not significant, and no obvious remelting is observed.

The evolution of the solid shell is shown in Figures 12 and 13. The overview of the solid-phase distribution on wide face shows an unevenness of shell formation. This unevenness attributes mainly to the specific flow pattern. As seen in Figure 13(c), a phenomenon of shell thinning along the Section II at a position 650 mm from meniscus occurs. The position of shell thinning coincides with the region of the transition from funnel-shape mold to straight mold, where the side jet flow impinges the solidification front of the wide face and remelting occurs there. Due to the corner effect, the solid shell of narrow face (Figure 13(e)) grows faster than that of wide face. If we use the isoline of $f_s = 0.3$ to define the shell thickness, the shell thickness at the mold exit of the narrow face is 28 pct larger than the average shell thickness at the mold exit of the wide face.

The numerical prediction is also compared with the experimentally measured shell thickness[3] based on a break-out shell, as shown in Figure 13. Due to some uncertainties of the experimental measurement and data acquisition method, *e.g.*, the operation delay and the duration of drainage are not clear, this comparison can only give a qualitative indication. The measured shell thickness shows a rough agreement with the simulated one. The measured position of solidification front is found to be in a range between the isoline of $f_s = 0.01$ and the isoline of $f_s = 0.3$. The trend of the shell evolution can be well predicted. The numerically predicted shell thickness at the mold exit is 41.7 pct of the slab thickness, which is different but close to the reported ~45 pct in the experiment. Considering the aforementioned uncertainties, this qualitative agreement is satisfied. For further quantitative comparison, a well-documented break-out shell of TSC with proper consideration of the operation delay and duration of drainage as was observed by Iwasaki and Thomas for a conventional slab casting[40] is desired.

The importance of considering the transport of latent heat in the moving and deforming solid shell (mushy zone) is also verified in this TSC. The above calculation has fully considered the advection term $\rho L \nabla \cdot \left(f_s \vec{u}_s \right)$. Here an additional calculation of the same TSC by ignoring the advection term is performed and compared with the former one with fully considered advection term. The comparison result is shown in Figure 14. The latter case predicts much thicker shell than the former case. The same conclusion as what we obtained from the 2D benchmark (Section III) is drawn: disregarding the advection term $\rho L \nabla \cdot \left(f_s \vec{u}_s \right)$ significantly overestimates the solid shell thickness. Making an integral of the solid phase formed in the whole TSC calculation domain, we find that the overestimation is about 94 pct.

V. DISCUSSION

A. *Importance of the Transport of Latent Heat*

The importance of the latent heat advection term ($\rho L \nabla \cdot \left(f_s \vec{u}_s \right)$) in the formulation of the energy equation for casting processes with the motion of solidified phase is numerically verified. The ignorance of this term would lead to a significant overestimation of the formation of solid phase. For example, the calculation of the 2D benchmark (Section III) shows that the above ignorance leads to an overestimation of 67.6 pct, and the calculation of 3D TSC (Section IV) shows an overestimation of 94 pct. The above quantities of the overestimation, which seem to be case dependent, may need further confirmation, desirably with assistance of some experiments. However, the fact of necessity to include this term in the numerical model is proven, and it is also confirmed by others.[22,23] To the authors' knowledge, the "equivalent heat capacity model,"[21] which did not consider the latent heat advection term, has successfully been applied in many casting processes where the solidified phase is stationary, *e.g.*, ingot and shape castings. According to

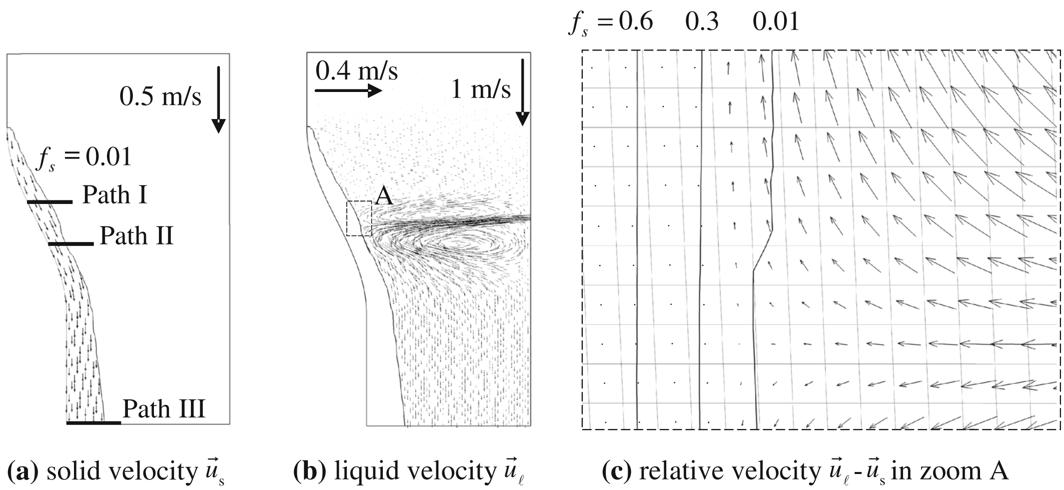

Fig. 3—Calculated solid (*a*) and liquid (*b*) velocities and interdendritic flow (*c*) in zoom A. In (a) and (b), the geometry in the vertical direction is scaled by 1/8, but in (c) it is scaled by 1/1. The result is shown for Case I.

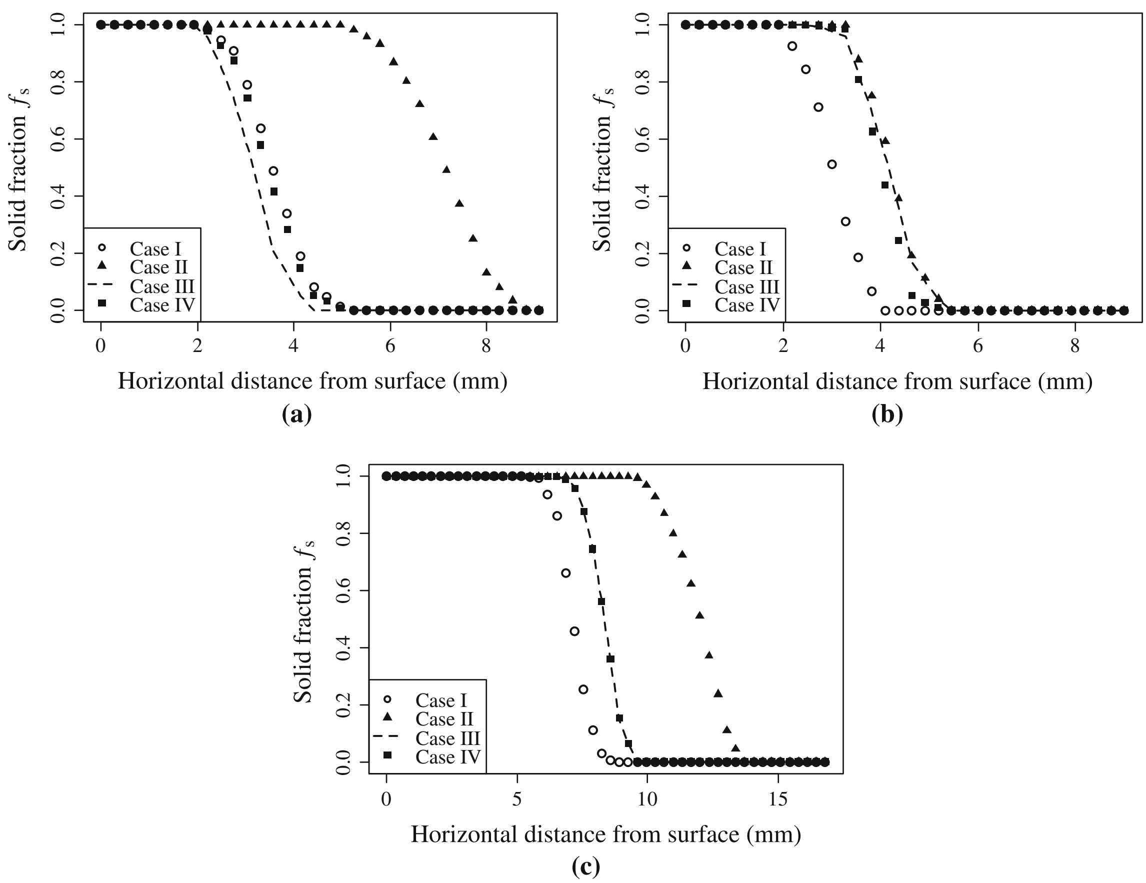

Fig. 4—Solid volume fraction distributions of different simulation cases along (*a*) Path I, (*b*) Path II, and (*c*) Path III. Positions of the paths are marked in Fig. 3(a).

current study, if this 'equivalent heat capacity model' is applied for TSC where the formation and motion of solid shell is important, modification by considering the latent heat advection must be made.

The current formulation of energy equation is slightly different from those in the literature.[26,27] The difference between the two models is the calculation of sensible enthalpies of the liquid and solid phases. In the literature, the liquid and solid phases are considered to have different sensible enthalpies, $h_\ell^{\mathrm{sensible}}$ and h_s^{sensible}. These are calculated according to the specific heats of each individual phase, $c_{p,\ell}$ and $c_{p,s}$, and the defined reference enthalpies, $h_{\mathrm{ref},\ell}$ and $h_{\mathrm{ref,s}}$, at the reference temperature, T_{ref}.

$$h_\ell^{\mathrm{sensible}} = h_{\mathrm{ref},\ell} + \int_{T_{\mathrm{ref}}}^{T} c_{\mathrm{p},\ell} \mathrm{d}T$$
$$h_{\mathrm{s}}^{\mathrm{sensible}} = h_{\mathrm{ref},s} + \int_{T_{\mathrm{ref}}}^{T} c_{\mathrm{p,s}} \mathrm{d}T. \qquad [17]$$

The total enthalpy of liquid phase, h_ℓ^{total}, is the sum of the sensible enthalpy, $h_\ell^{\mathrm{sensible}}$, and the latent heat L; while the total enthalpy of solid phase, $h_{\mathrm{s}}^{\mathrm{total}}$, is equal to the sensible enthalpy, $h_{\mathrm{s}}^{\mathrm{sensible}}$. According to this definition, the released energy by solidification from liquid to solid is $\left(h_\ell^{\mathrm{total}} - h_{\mathrm{s}}^{\mathrm{total}}\right)$, which should be equal to the latent heat, *i.e.*, L, or

$$h_{\mathrm{ref},\ell} - h_{\mathrm{ref,s}} + \int_{T_{\mathrm{ref}}}^{T} \left(c_{\mathrm{p},\ell} - c_{\mathrm{p,s}}\right) \mathrm{d}T = 0. \qquad [18]$$

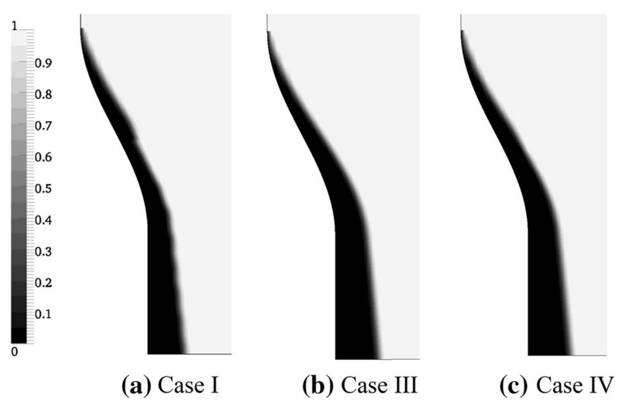

Fig. 5—Comparison of the numerically predicted shell thickness profiles between Case I (a), Case III (b), and Case IV (c). Figures are zoomed in the domain of the solid shell to get more details.

In reality, however, the condition of Eq. [18] would never be easily fulfilled when one considers that the solidification occurs in a temperature interval and that $c_{\mathrm{p},\ell}$ and $c_{\mathrm{p,s}}$ are not equal, no matter how one defines the reference quantities of $h_{\mathrm{ref},\ell}$, $h_{\mathrm{ref,s}}$, T_{ref}. In order to solve this problem, a special numerical treatment[22,23] must be carried out by including an additional term (or terms) in the energy equation. The formulation of the additional term depends on the definition of the reference quantities of $h_{\mathrm{ref},\ell}$, $h_{\mathrm{ref,s}}$, T_{ref}, and the values of $c_{\mathrm{p},\ell}$ and $c_{\mathrm{p,s}}$. This consideration would increase the complexity of the model implementation and application. In the current model, we assume $\left(h_\ell^{\mathrm{sensible}} = h_{\mathrm{s}}^{\mathrm{sensible}}\right)$ by setting $(h_{\mathrm{ref},\ell} = h_{\mathrm{ref,s}})$ and $(c_{\mathrm{p},\ell} = c_{\mathrm{p,s}})$. $c_{\mathrm{p},\ell}$ and $c_{\mathrm{p,s}}$ are not necessarily constant. The model is significantly simplified, as Eq. [18] is unconditionally fulfilled.

B. *Motion of Solid Phase*

To estimate the solid velocity, $\vec{u}_{\mathrm{s}}$, due to the funnel-type mold, an incompressible rigid viscoplastic model with certain simplification is implemented here. The thermal shrinkage of the strand inside the mold, the mechanical bulging between support rolls out of the mold, the body force induced deformation, and their influence on the inner flow are considered to be negligibly small. This velocity field estimated by the incompressible rigid viscoplastic model is only used for the treatment of the advection of latent heat due to the large deformation of the solid shell in the region of the funnel-type mold. The change of heat transfer at the strand–mold interface due to all kinds of mechanical deformations of the strand and the formation of air gap, as mentioned above, is considered by an experimentally determined distribution profile of heat flux.[3] Full thermo-mechanical models such as those in the literature[41,42] would enhance the model capability.

Another important feature of the deforming mushy zone is its non-divergence-free ($\nabla \cdot \vec{u}_{\mathrm{s}} \neq 0$) behavior of deformation.[43] The mushy zone is a combination of the dendritic structure (skeleton) and the interdendritic

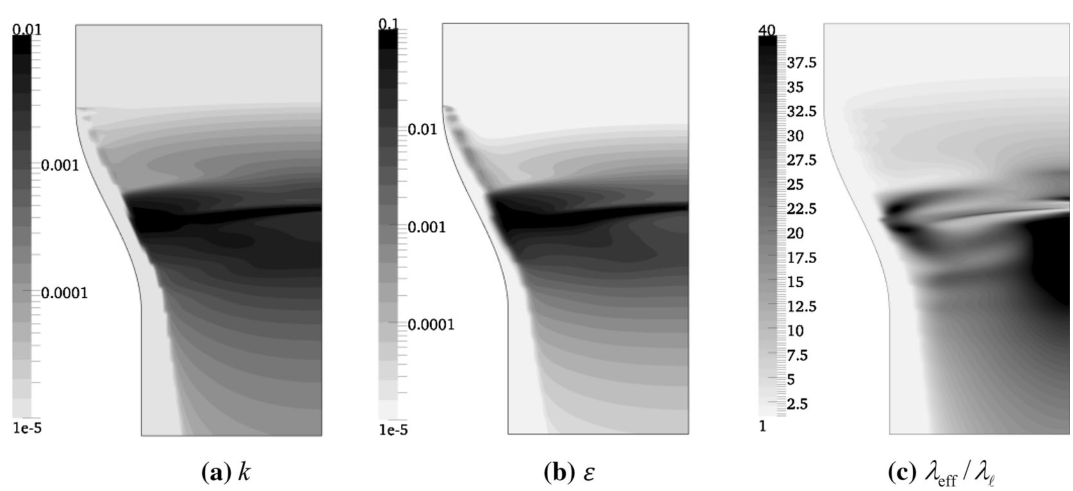

Fig. 6—Calculated distributions of turbulence kinetic energy (a), dissipation rate (b), and normalized effective thermal conductivity (c) of Case I.

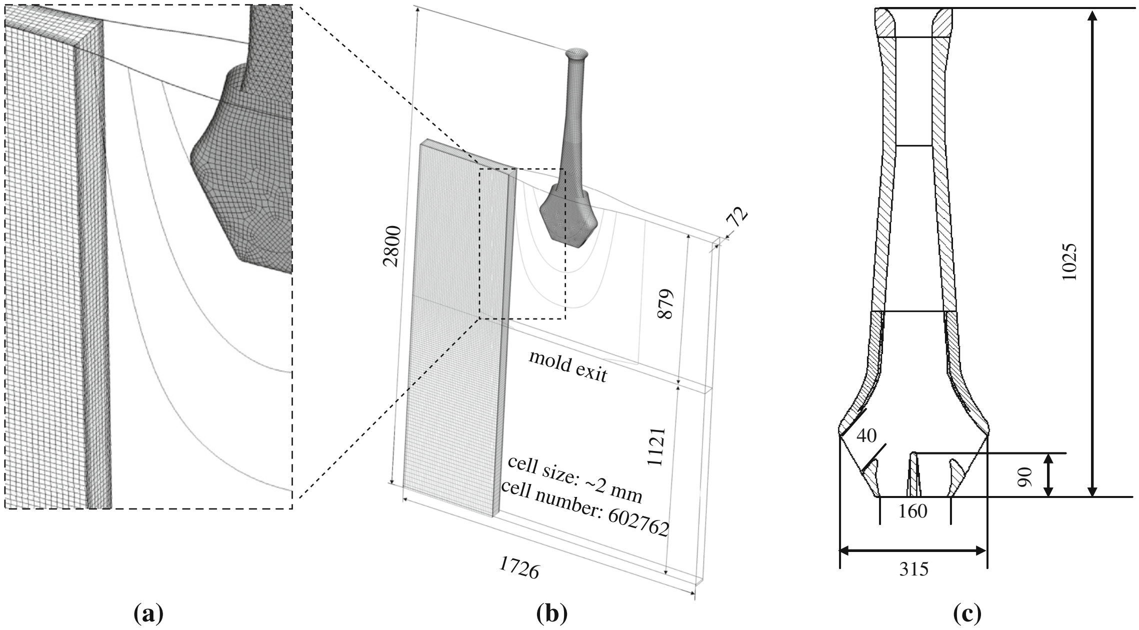

Fig. 7—Calculation domain of the thin slab casting (TSC).

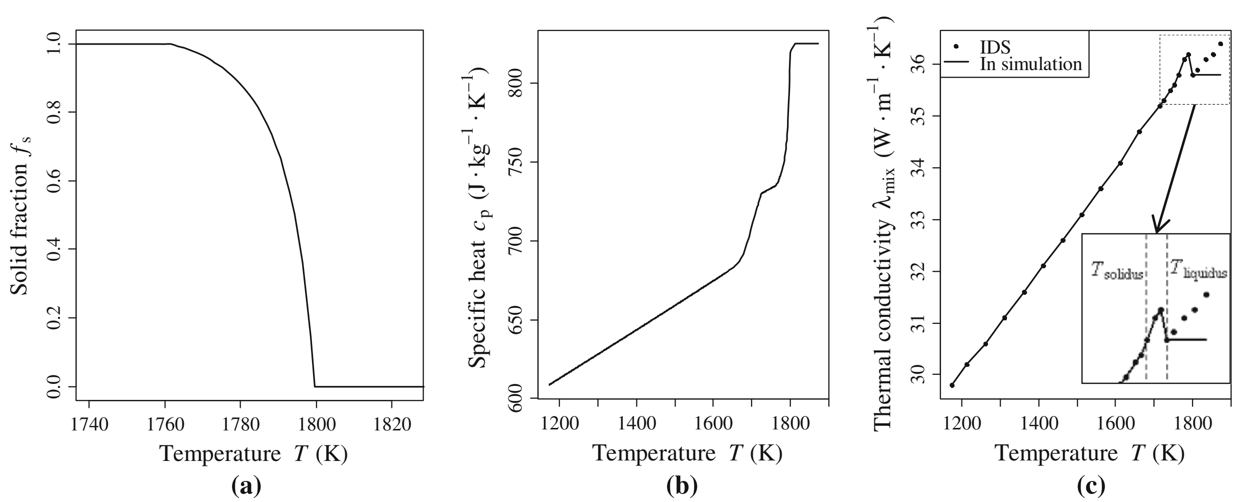

Fig. 8—Temperature-dependent material properties/data from IDS. (*a*) f_s–T curve, (*b*) specific heat, and (*c*) thermal conductivity. An effective thermal conductivity by considering the effect of convection was read from IDS (dots). Therefore, we take a value read at $T_{liquidus}$ as the physical value of thermal conductivity, and assume a constant thermal conductivity for the liquid melt (solid line).

melt. When the mushy zone is subject to deformation, the interdendritic space can either be enlarged by sucking in external melt or reduced by squeezing out the interdendritic melt. Evidently, this non-divergence-free deformation would, according to Eqs. [7]–[8b], significantly contribute to the source term of the energy conservation equation, hence influencing the final prediction of the solid phase formation. Unfortunately, this feature is not considered in the current model. Even the recently proposed mechanical models for conventional slab or thin slab castings fail to consider this feature. Further modeling efforts are required.

C. *Calculation Accuracy and Calculation Efficiency*

The mesh and the time-step dependencies of the numerical solution were examined. A low latent heat relaxation factor (0.05), along with a relatively large number of iterations (50 per time-step), enabled the use of relatively large time steps without the problem of divergence. It was shown that the increase in time-step did not influence the final steady-state solution. To improve the calculation accuracy, authors[37,39] previously confirmed the necessity to use separate refinement regions for the temperature and solid fraction fields. Being an extended topic itself, the study of mesh dependency of the solution is not presented here. Consecutive mesh refinements were thereby made based on the error analysis of the energy equation. It must be stated that we even though used an initial cell size of 2 mm, later on refined to as small as 0.4 mm locally, for the 3D TSC, a grid-independent result is still not achieved regarding various fine details of the mushy zone. As we can see from Figure 11, the front of mushy zone confronting relatively strong flow is still not fully converged, despite ca. 6 grid points being used in the mushy zone. However, the global solidification sequence, and in particular the predicted final shell thickness at the mold exit, remains stable with regard to the further grid refinement. The calculation cost is still too high. One calculation of the full 3D TSC lasts 2 weeks. This high calculation cost is not due to the implementation in the OpenFOAM®. A previous work of the authors[19] has implemented the same model in another CFD code, ANSYS-Fluent, for calculating the conventional slab casting, and a same conclusion was drawn. It means that this model is unrealistic for online troubleshooting of industry processes, but it is acceptable if we use it to perform the laboratory investigation and a limited parameter study for the purpose of parameter optimization and for the purpose of achieving a fundamental understanding of the process.

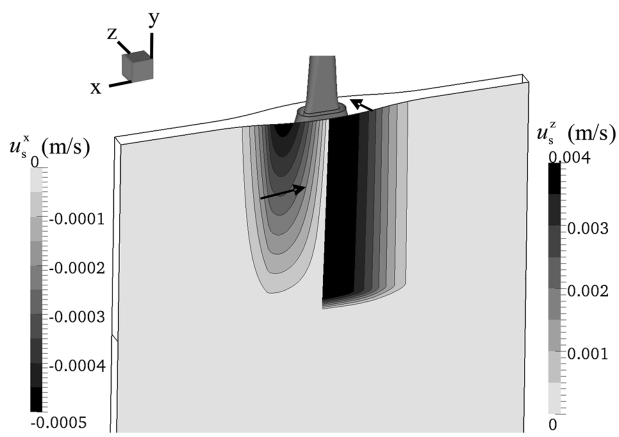

Fig. 9—Applied moving boundary condition on the wide face: horizontal velocity components in the wide face direction (left) and thickness (right) direction.

D. *Model Validation*

Although no direct experimental measurement with the current TSC settings is performed, indirect model validations against experiments and literature were carried out. (1) The qualitative agreement of the predicted shell thickness with the experiment of Camporredondo *et al.*[3] gives an indication that the trend of shell evolution can be well predicted by the current model. (2) A similar model was previously applied to a conventional slab casting[19] and validated against the measurement on the break-out shell.[20] The predicted shell thickness is in good agreement with the measurement at both wide and narrow faces. (3) A comparison of the current simulation with those performed by Liu *et al.*[18] is made. The models and TSC settings used are similar. The calculation of Liu predicted the average

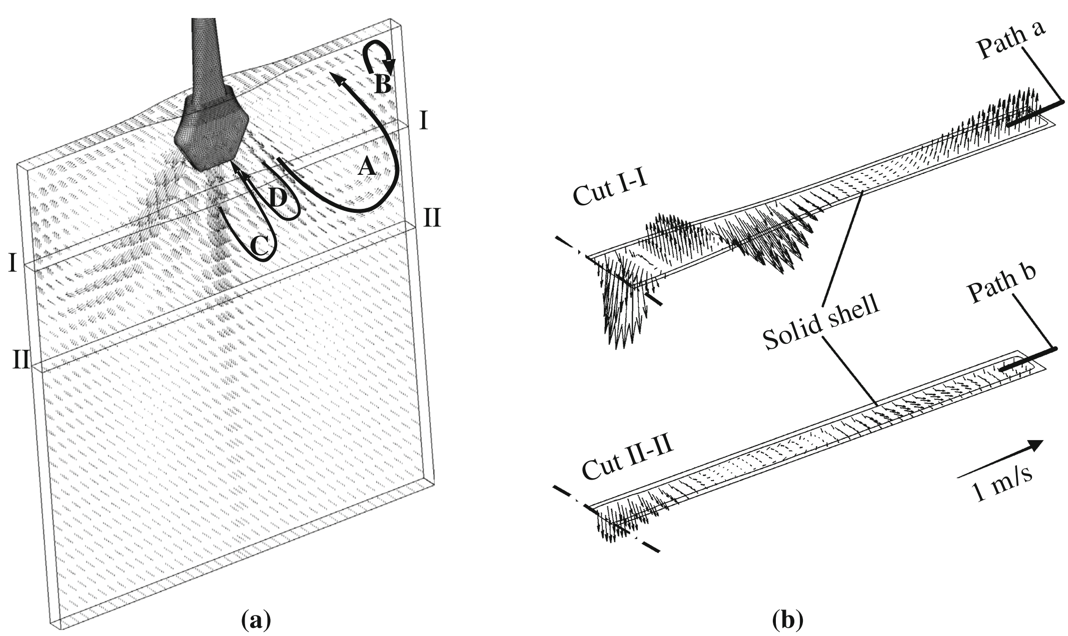

Fig. 10—Flow pattern of a TSC. (*a*) 3D distribution of the velocity vector field; (*b*) flow direction at a horizontal Cut I–I (inside the mold) and at Cut II–II (mold exit).

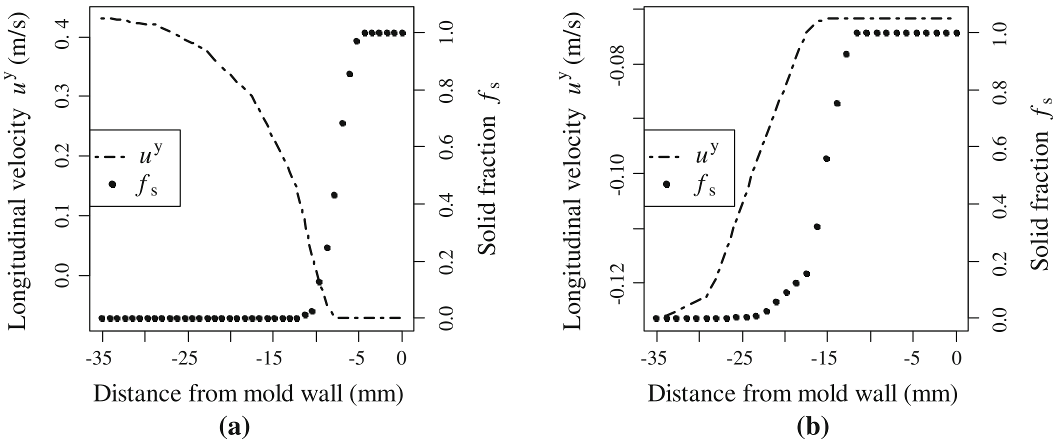

Fig. 11—Detailed velocity (u^y component) and solid volume fraction distribution along (*a*) Path a and (*b*) Path b (marked in Fig. 10(b)) across the mushy zone at the narrow face near the wall.

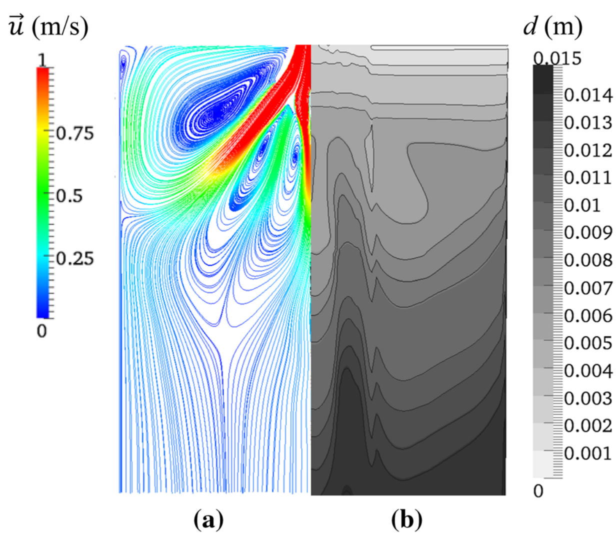

Fig. 12—Analysis of the influence of flow pattern on the solid shell formation: (*a*) the stream lines in the center-plane colored with the melt velocity $\vec{u}$; (*b*) distribution of the shell thickness on the wide face (a plane projection of the 3D strand surface on a 2D view).

shell thickness at the mold exit to be 38.9 pct of the slab thickness, which is similar to (but slightly smaller than) the current calculation of 41.7 pct of the slab thickness. Further evolution efforts are desired involving comparison with the well-controlled laboratory experiments or with a well-documented break-out shell with proper consideration of the operation delay and duration of drainage.[40]

VI. CONCLUSIONS

The enthalpy-based mixture solidification model is verified to be suitable for the calculation of solidification during thin slab casting (TSC). The following two key features for TSC among many others are considered.

1. Turbulent flow and its influence on the evolution of the solid shell. The hydrodynamic interaction between the flow and the solidifying mush zone is modeled by a volume-averaged parameter, permeability, which is a function of the local solid fraction and a microstructural parameter, *i.e.*, primary dendrite arm space. The turbulence-induced thermal mixing and its influence on the solidification are also taken into account.
2. Advection of latent heat due to the motion and deformation of solid shell in the thin slab casting with a funnel-type mold. An incompressible rigid visco-plastic model is used to estimate the motion of the solid phase.

Based on a numerical parameter study on a 2D benchmark and an illustrative simulation of TSC, the following findings are obtained.

1. In order to model the TSC, the advection of the latent heat due to the motion of the solid shell must be properly treated. Models which ignore the advection of latent heat due to the motion of the solid shell would significantly overestimate the formation of the solid shell.
2. Highly turbulent jet flow impinging the solidification front suppresses the local solidification. Although it was found that the transport of the superheat by the jet flow to the solidification front leading to local remelting might be the important reason responsible for this phenomenon,[38] the current study shows that the effect of turbulence-induced thermal mixing seems to play more important role in the suppression of solid shell. For this point, further verification is needed.

Evaluation of the simulation result of the TSC by comparison with the measurement on the so-called break-out shell was made, and a reasonable agreement was obtained. Nevertheless, further evolution efforts based on the well-controlled laboratory experiments or on a well-documented break-out shell with proper consideration of the operation delay and duration of drainage are desired.

Based on the current computer capacity, calculation cost is still too high. The enthalpy-based mixture

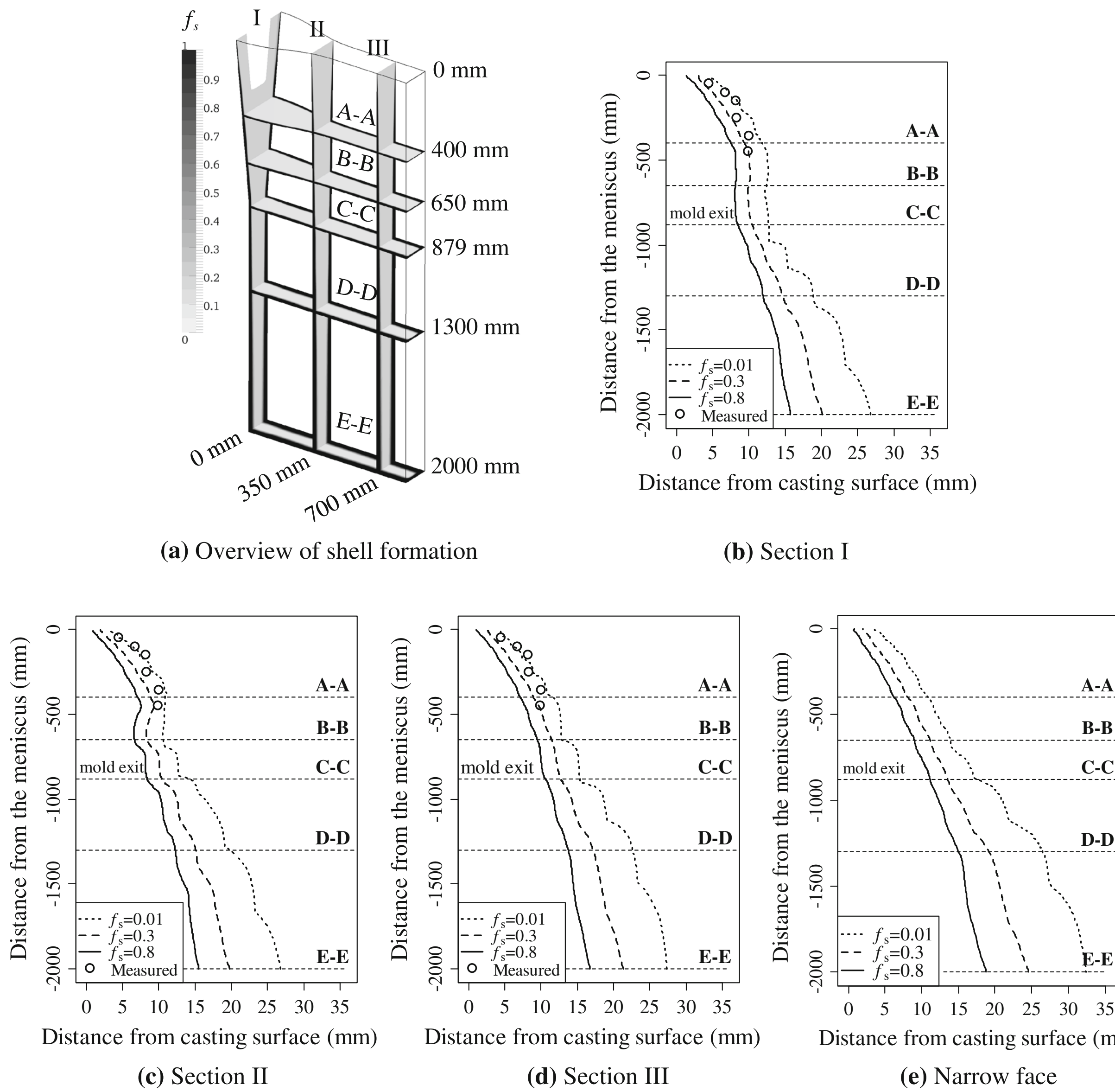

Fig. 13—(*a*) Evolution of the shell thickness at various transverse and vertical sections. Profiles of the volume fraction of solid along the casting direction at different vertical sections: (*b*)–(*d*) on wide face; (*e*) on narrow face. Marked points in (b)–(d) are measured shell thickness from a break-out shell[3].

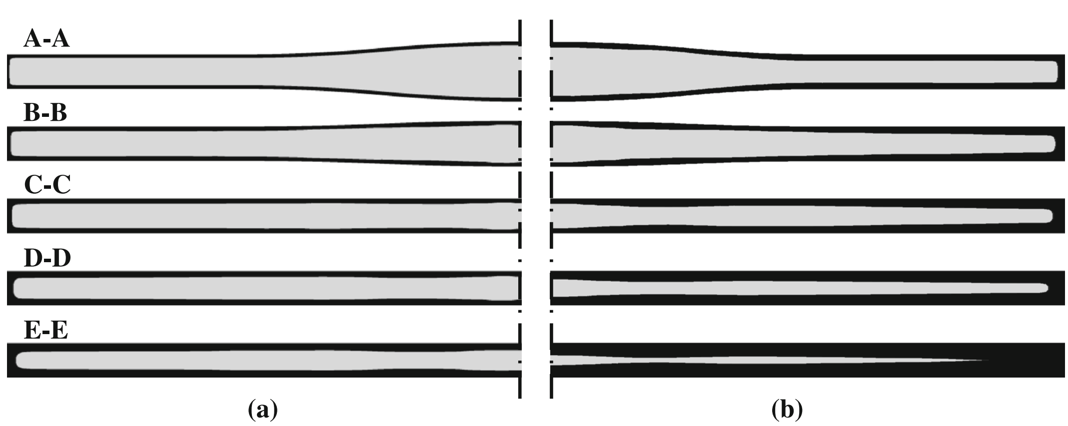

Fig. 14—Comparison of the solidified shell thickness ($f_s = 1$) for the simulation (*a*) including the latent heat advection term ($\rho L \nabla \cdot \left(f_s \vec{u}_s\right)$) and (*b*) excluding it.

solidification model is not suitable for the online troubleshooting of the industry problem, but it can be applied for the purpose of achieving a fundamental understanding of the process on the basis of the process simulation and for the purpose of process optimization by means of a parameter study.

ACKNOWLEDGMENTS

The financial support by RHI AG, the Austrian Federal Ministry of Economy, Family and Youth and the National Foundation for Research, Technology and Development is gratefully acknowledged. The authors acknowledge the fruitful discussions with Professor Brian G. Thomas, University of Illinois at Urbana-Champaign, USA, and Dr. Christian Chimani, Austrian Institute of Technology, Austria.

NOMENCLATURE

c_{p}	Specific heat of liquid–solid mixture (J kg^{-1} K^{-1})
$C_{1\varepsilon}$,$C_{2\varepsilon}$,C_{μ}	Constants of the standard k–ε model (1)
E	Young's modulus (N m^{-2})
f_{ℓ},f_{s}	Volume fraction of liquid and solid phases (1)
$f_{\mathrm{s}}^{\mathrm{integral}}$	Total solid phase in the calculation domain (1)
G	Shear production of turbulence kinetic energy (kg m^{-1} s^{-3})
h	Sensible enthalpy of liquid–solid mixture (J kg^{-1})
h_{ref}	Reference enthalpy at temperature T_{ref} (J kg^{-1})
$h_{\ell}^{\mathrm{sensible}}$	Sensible enthalpy of liquid phase (J kg^{-1})
$h_{\mathrm{s}}^{\mathrm{sensible}}$	Sensible enthalpy of solid phase (J kg^{-1})
$h_{\ell}^{\mathrm{total}}$	Total enthalpy of liquid phase (J kg^{-1})
$h_{\mathrm{s}}^{\mathrm{total}}$	Total enthalpy of liquid phase (J kg^{-1})
H	Total enthalpy of liquid–solid mixture (J kg^{-1})
H_{ℓ},H_{s}	Total enthalpy of liquid or solid phase (J kg^{-1})
HTC	Heat transfer coefficient between mold and casting (W m^{-2} K^{-1})
k	Turbulence kinetic energy per unit of mass (m^2 s^{-2})
k_{p}	Partition coefficient of binary alloy (1)
K	Permeability (m^2)
L	Latent heat (J kg^{-1})
$\vec{n}_{\mathrm{f}}$	Unit vector normal to the curved mold surface (1)
$\vec{n}_{\mathrm{z}}$	Unit vector normal in casting direction (1)
p	Pressure (N m^{-2})
PDAS	Primary dendrite arm space (m)
$\mathrm{Pr}_{\mathrm{t,h}}$	Prandtl no. for energy equation (1)
$\mathrm{Pr}_{\mathrm{t,k}}$	Prandtl no. for turbulence kinetic energy k (1)
$\mathrm{Pr}_{\mathrm{t},\varepsilon}$	Prandtl no. for turbulence dissipation rate ε (1)
S_{e}	Source term for energy equation (J m^{-3} s^{-1})
$\vec{S}_{\mathrm{mom}}$	Source term for momentum equation (kg m^{-2} s^{-2})
t	Time (s)
T	Temperature (K)
T_{ext}	External mold surface temperature
T_{f}	Melt point of pure solvent (K)
T_{inlet}	Inlet temperature (K)
T_{liquidus}	Liquidus temperature of alloy (K)
T_{ref}	Reference temperature for h_{ref} (K)
T_{solidus}	Solidus temperature of alloy (K)
$\vec{u}(u^x,u^y,u^z)$	Velocity of the liquid–solid mixture (m s^{-1})
$\vec{u}_{\mathrm{inlet}}$	Inlet velocity (m s^{-1})
$\vec{u}_{\mathrm{pull}}$	Casting velocity (m s^{-1})
$\vec{u}_{\ell}(u_{\ell}^x,u_{\ell}^y,u_{\ell}^z)$	Liquid velocity (m s^{-1})
$\vec{u}_{\mathrm{s}}(u_{\mathrm{s}}^x,u_{\mathrm{s}}^y,u_{\mathrm{s}}^z)$	Solid velocity (m s^{-1})
$\vec{u}_{\mathrm{s}}^{\mathrm{surface}}$	Moving surface velocity (m s^{-1})
$\vec{\delta}$	Displacement vector (m)
Δx	Mesh size (m)
ε	Turbulence dissipation rate per unit of mass (m^2 s^{-3})
λ	1$^{\mathrm{st}}$ Lamé parameter (N m^{-2})
λ_{mix}	Thermal conductivity of liquid–solid mixture (W m^{-1} K^{-1})
λ_{eff}	Effective thermal conductivity due to turbulence (W m^{-1} K^{-1})
λ_{t}	Turbulence thermal conductivity (W m^{-1} K^{-1})
$\rho(=\rho_{\ell}=\rho_{\mathrm{s}})$	Density (kg m^{-3})
μ	2$^{\mathrm{nd}}$ Lamé parameter (N m^{-2})
μ_{eff}	Dynamic effective viscosity due to turbulence (kg m^{-1} s^{-1})
μ_{ℓ}	Dynamic liquid viscosity (kg m^{-1} s^{-1})
μ_{t}	Dynamic turbulence viscosity (kg m^{-1} s^{-1})
v	Poisson's ratio (1)

REFERENCES

1. R. Bruckhaus and R. Fandrich: *Trans. Indian Inst. Met.*, 2013, vol. 66, pp. 561–66.
2. R.Y. Yin and H. Zhang: *Iron Steel (Peking)*, 2011, vol. 46, pp. 1–9.
3. J.E. Camporredondo-S, A.H. Castillejos-E, F.A. Acosta-G, E.P. Gutierrez-M, and M.A. Herrera-G: *Metall. Mater. Trans. B*, 2004, vol. 35B, pp. 541–60.
4. J.E. Camporredondo-S, FA Acosta-G, AH Castillejos-E, EP Gutierrez-M, and R Gonzalez: *Metall. Mater. Trans. B*, 2004, vol. 35B, pp. 561–73.
5. T.G. O'Connor and J.A. Dantzig: *Metall. Mater. Trans. B*, 1994, vol. 25B, pp. 443–57.
6. R.D. Morales, Y. Tang, G. Nitzl, C. Eglsäeer, and G. Hackl: *ISIJ Int.*, 2012, vol. 52, pp. 1607–15.
7. S. Garcia-Hernandes, R.D. Morales, and E. Torres-Alonso: *Ironmak. Steelmak.*, 2010, vol. 37, pp. 360–68.
8. M.M. Yavuz: *Steel Res. Int.*, 2011, vol. 82, pp. 809–18.

9. J.A. Kromhout, E.R. Dekker, M. Kawamoto, and R. Boom: *7th European Continuous Casting Conference, Session 8: Mould Performance and Initial Solidification,* Düsseldorf, 2011, p. S8.1.
10. X. Tian, B. Li, and J. He: *Metall. Mater. Trans. B*, 2009, vol. 40B, pp. 596–604.
11. J. Park, B.G. Thomas, I. Samaraseka, and U. Yoon: *Metall. Mater. Trans. B*, 2002, vol. 33B, pp. 425–36.
12. K. Cukierski and B.G. Thomas: *Metall. Mater. Trans. B*, 2008, vol. 39B, pp. 94–107.
13. H. Nam, H. Park, and J. Yoon: *ISIJ Int.*, 2000, vol. 40, pp. 886–92.
14. E. Torres-Alonso, R.D. Morales, and S. Garcia-Hernandez: *Metall. Mater. Trans. B*, 2010, vol. 41B, pp. 675–90.
15. H. Park, H. Nam, and J. Yoon: *ISIJ Int.*, 2001, vol. 41, pp. 974–80.
16. S.L. Choi, K.J. Ryu, and H.S. Park: *Met. Mater. Int.*, 2002, vol. 8, pp. 527–33.
17. X. Tian, F. Zou, B. Li, and J. He: *Metall. Mater. Trans. B*, 2010, vol. 41B, pp. 112–20.
18. H Liu, C Yang, H Zhang, Q Zhai, and Y Gan: *ISIJ Int.*, 2011, vol. 51, pp. 392–401.
19. C. Pfeiler, B.G. Thomas, M. Wu, A. Ludwig, and A. Kharicha: *Steel Res. Int.*, 2008, vol. 79, pp. 599–607.
20. B.G. Thomas, R.O. O'Malley, and D. Stone: in *Proc. MCWASP VIII*, B.G. Thomas and C. Beckermann, eds., TMS Publications, Warrendale, PA, 1998, pp. 1185–1192.
21. J.S. Hsiao: *Numer. Heat Transf.*, 1985, vol. 8, pp. 653–66.
22. P.R. Chakraborty and P. Dutta: *Metall. Mater. Trans. B*, 2011, vol. 42B, pp. 1075–79.
23. B. Sarler, R. Vertnik, and K. Mramor: *Proc. MCWASP XIII: IOP Conf. Series: Materials Sci. Eng*, A. Ludwig, M. Wu, and A. Kharicha, eds., Schladming, 2012. doi:10.1088/1757-899X/33/1/012012.
24. V.R. Voller and C. Prakash: *Int. J. Heat Mass Transf.*, 1987, vol. 30, pp. 1709–19.
25. V.R. Voller, A.D. Brent, and C. Prakash: *Int. J. Heat Mass Transf.*, 1989, vol. 32, pp. 1719–37.
26. V.R. Voller, A.D. Brent, and C. Prakash: *Appl. Math. Model.*, 1990, vol. 14, pp. 320–26.
27. P.J. Prescott and F.P. Incropera: *Transp. Phenom. Mater. Proc. Manuf. ASME HTD*, 1994, vol. 280, pp. 59–69.
28. P.J. Prescott and F.P. Incropera: *J. Heat Transf.*, 1994, vol. 116, pp. 735–41.
29. P.J. Prescott, F.P. Incropera, and D.R. Gaskell: *Trans. ASME*, 1994, vol. 116, pp. 742–49.
30. P.J. Prescott and F.P. Incropera: *Trans. ASME*, 1995, vol. 117, pp. 716–24.
31. W. Kurz and D.J. Fisher: *Fundamentals of Solidification*, 4th ed., Trans Tech Publications Ltd, Dürnten, 1998, pp. 280–88.
32. J. Miettinen, S. Louhenkilpi, H. Kytönen, and J. Laine: *Math. Comput. Simul.*, 2010, vol. 80, pp. 1536–50.
33. J.P. Gu and C. Beckermann: *Metall. Mater. Trans.*, 1999, vol. 33A, pp. 1357–66.
34. OpenFOAM® V2.2.0 Documentation. http://www.openfoam.org/archive/2.2.0/docs/.
35. W.S. Slaughter: *The Linearized Theory of Elasticity*, Birkhäuser, Boston, 2002, pp. 1–514.
36. P.J. Roache: *Fundamentals of Computational Fluid Dynamics*, Hermosa Publishers, New Mexico, 1998, pp. 1–135.
37. A. Vakhrushev, M. Wu, A. Ludwig, Y. Tang, G. Hackl, and G. Nitzl: *Proc. MCWASP XIII: IOP Conf. Series: Materials Sci. Eng*, A. Ludwig, M. Wu, A. Kharicha, eds., Schladming, 2012. doi: 10.1088/1757-899X/33/1/012014.
38. S. Koric, B.G. Thomas, and V.R. Voller: *Numer. Heat Transf. B Fundam.*, 2010, vol. 57, pp. 396–413.
39. A. Vakhrushev, A. Ludwig, M. Wu, Y. Tang, G. Nitzl, and G. Hackl: *Proc. OSCIC'12*, London, 2012, pp. 1–18.
40. J. Iwasaki and B.G. Thomas: *Proc. Materials Properties, Characterization, and Modeling*, TMS Annual Meeting, 2012, pp. 355–362.
41. C. Li and B.G. Thomas: *Metall. Mater. Trans. B*, 2004, vol. 35B, pp. 1151–72.
42. A. Koric, L.C. Hibbeler, and B.G. Thomas: *Int. J. Numer. Methods Eng.*, 2009, vol. 78, pp. 1–31.
43. M. Wu, J. Domitner, and A. Ludwig: *Metall. Mater. Trans. A*, 2012, vol. 43A, pp. 945–963.